Heusler alloy-based heat engine using pyroelectric conversion for small-scale thermal energy harvesting

Mickaël Null Lallart, Linjuan Yan, Hiroyuki Miki, Gaël Sebald, Gildas Diguet, Makoto Ohtsuka, Manfred Kohl

Heusler Alloy-Based Heat Engine using Pyroelectric Conversion for Small-Scale Thermal Energy Harvesting

Mickaël LALLART[1,2,3], Linjuan YAN[1,3], Hiroyuki MIKI[1], Gaël SEBALD[3], Gildas DIGUET[3], Makoto OHTSUKA[4] and Manfred KOHL[5]

[1] *Institute of Fluid Science, Tohoku University, Sendai, Japan*
[2] *Univ. Lyon, INSA-Lyon, LGEF EA 682, F-69621, France*
[3] *ELyTMaX UMI 3757, CNRS – Université de Lyon – Tohoku University, International Joint Unit, Tohoku University, Sendai, Japan*
[4] *Institute of Multidisciplinary Research for Advanced Materials, Tohoku University, 2-1-1, Katahira, Aoba-ku, Sendai 980–8577, Japan*
[5] *Institute of Microstructure Technology (IMT), Karlsruhe Institute of Technology (KIT), Hermann-von-Helmholtz-Platz 1 76344 Eggenstein-Leopoldshafen*

Abstract

As an alternative to thermoelectric generators, heat engines show great interest thanks to their ability to convert temperature spatial gradient into time-domain temperature variations or vibrations. To this end, MultiPhysic Memory Alloys (MPMAs), combining shape memory characteristics with ferromagnetic properties, provide significant attractive characteristics such as sharp transition with reduced hysteresis as well as magnetic properties enabled by heating, thus allowing easier device development and implementation. In this study, we report the development of a heat engine for small-scale energy harvesting where the MPMA transfers its heat to a pyroelectric element that provides thermal to electrical energy conversion, yielding a more direct energy conversion path compared to conventional electromechanical heat engines. Furthermore, thermally decoupling the pyroelectric element from the MPMA allows a faster cooling of the latter, accounting for higher variation frequency. Compared to the use of electromagnetic transduction through a coil attached to the moving MPMA, this approach is shown to provide 3 to 9 times more power density (according to considered volume), with theoretical potential gains from 8 to 25 with the use of nonlinear electrical interfaces.

Keywords: energy harvesting, heat engine, shape memory alloy, ferromagnetism, pyroelectric, thermal

1. Introduction

With the rise of microwatt and sub-microwatt electronic components and sensors, autonomous wireless devices and networks are experiencing a rapid development both at scientific and industrial scales, notably boosted by promises of the "Internet of Things" concept. The wide deployment of such connected and interconnected systems however raises the issue of ensuring stable, long-lasting and reliable power supply. While conventional batteries are mainly employed, they feature

*Corresponding author - mickael.lallart@insa-lyon.fr / Orcid ID: 0000-0002-6907-5946

severe limitations in application cases where the apparatus is intended to operate for long time in confined and/or relatively harsh environments. More precisely, recent trends have shown a shift of paradigm, where the limitations of batteries are no longer related to their initial stored energy but to their leakage that yields energy losses before it can be effectively used [1]. Such leakage is even more important under moderate to high temperatures for instance. As an example, at 60 $^\circ$C, Li-Ion battery packs lose more than half of their energy within one year [2], preventing their use in remote or barely accessible locations (*e.g.*, Tire Pressure Monitoring Systems [3]).

Under such circumstances, providing reliable energy source can be done considering the surrounding sources directly available from the close environment. Once converted into electrical energy, these sources can sustainably supply the device. This has led to the concept of small-scale "energy harvesting" that has been, under its modern form, under investigation for almost two decades, with outcomes in the field of energy, transportation [3], civil engineering [4], biomedical applications [5] and general sensing networks [6] for instance. In this framework, typical microgenerators scavenging energy from their close environment, with dimensions from millimeter scale to centimeter scale, can provide a few microwatts to a few milliwatts of output power to supply electronic components. Many energy sources can be under consideration according to the operating environment, such as solar or vibrations [7, 8]. However, thermal energy, that can be seen as the basic energy source, is widely available especially in the form of temperature gradients [9].

Converting temperature gradient into electricity can typically be done through thermoelectric modules (also referred as *ThermoElectric Generators* - TEG) [10, 11] that exploit Seebeck effect [12]. However, such materials show strong drawbacks in terms of input energy, as their high thermal conductivity prevents from effectively maintaining temperature gradient across the material in realistic applications [13], and necessitating the use of bulky heat exchangers that dramatically reduce the power density of this class of microgenerators. For example, while the footprint of Micropelt™ TGP module is only $15 \times 10 \times 9.3$ mm^3, achieving 1.7 mW for a hot side temperature of 50 $^\circ$C (cold side being at room temperature) necessitates the use of a $50 \times 43.1 \times 16.51$ mm^3 heat exchanger, hence increasing the device volume by a factor greater than 25 and reducing the actual power density to 46 μW.cm^{-3} [14].

Alternative solutions to overcome such limitations have been proposed through the use of heat engines, able to convert a temperature gradient into a mechanical motion (and thus local temperature time-domain variations). Among possible implementations of such systems using for instance Stirling engine ([15]), thermolytic osmotic heat engines ([16]) or thermoacoustic devices ([17]) which show limited integration potentials at small-scale, phase transitions in dedicated materials are an effective means to trigger mechanical vibrations or rotation from a temperature gradient (although other singular concepts have also been reported, such as bimetallic strips [18]). Thermally activated phase transitions can be obtained through gas-liquid transition [19] or structural phase transition of conventional Shape Memory Alloys (SMA) [20, 22] for instance, but the most efficient

approach at small scale lies in using the ferromagnetic transition of magnetic materials [23], as the associated solid state transition allows significant integration potentials. While ferromagnetic heat engine concepts have been devised for more than a century [24–26], their actual application in small scale systems coupled with proper energy conversion materials is still recent. Advanced solutions using materials combining both SMA and ferromagnetic behaviors (*Ferromagnetic Shape Memory Alloys* - FSMA) were thus demonstrated [27, 28]. Some of the reported concepts even revealed power densities competing with conventional TEGs [29], while showing further room for improvement thanks to up-scaling effects [30]. Yet, thermal gradient energy harvesting through heat engines is still at very low TRL (Technology Readiness Level) and requires more conceptual and technical developments for providing reliable and cost-effective solutions. In particular, one of the main limitations of current ferromagnetic and FSMA heat engines lies in the fact that material magnetic behavior is decreasing with temperature due to the sole second order ferromagnetic transition. In order to enable mechanical displacement, this necessitates the use of magnetizing elements (*e.g.*, magnets) close or in contact to the hot source. Such a constraint makes the device design quite complex, and may not be cost-effective as high-temperature magnets are quite expensive and/or do not provide significant magnetic flux density. While high performance magnets able to work efficiently up to 230 $^{\circ}$C (through addition of Dysprosium or Terbium for instance in the case of neodymium magnets) can be commercially found, such as the *AH* grade ([31]), their actual price may compromise the need of cost-affordable solutions to provide economically viable alternatives to conventional batteries. For example, raw Dysprosium cost is 5-10 times higher than that of Neodymium ([32, 33]).

Recently, a class of Heusler alloys [34] featuring metamagnetic behavior (*e.g.*, Ni-Mn-Co-In alloys [35]) has been demonstrated to provide attractive properties to overcome these limitations. Particularly, such materials show an initial gain of magnetization with the temperature, thanks to a reversed martensitic to austenite structural phase transition. Like FSMAs, such compounds allow interdependent link between thermal, magnetic and structural aspects, and can thus be considered as a *MultiPhysic Memory Alloy* (MPMA). However, their particular magnetic properties triggered at high temperature permit using magnets on the cold side of the harvester, therefore significantly relaxing design constraints and allowing new concepts to be exploited [35]. Additionally, while it might be thought that Heusler alloy-based heat engines may be prone to thermal cycling effects that would compromise their good operations, it shall be noted that for such applications only partial transformation occurs, hence limiting the structural changes. Additionally, Ni-Mn based compositions as investigated in the present study show much weaker dependence to thermal cycles (with changes of the transition temperature of a few K only and similar hysteresis width after thousand cycles - [36, 37]) compared to other alloys such as Co-Cr-Ga-Si, which can experience total suppression of martensitic transformation after a few cycles ([38]).

Nevertheless, whatever the considered effect behind proposed heat engines in the literature, the

large majority relies on electromechanical energy conversion (piezoelectric, magnetic and so on) from the mechanical oscillations, necessitating an additional step in the energy flow therefore limiting the device efficiency. Direct thermal transfer and its conversion into electricity, would therefore provide a more straightforward energy conversion path and thus better performance. Noting that heat engines not only provide conversion of a DC temperature gradient into a mechanical oscillation but also convert this thermal input into a time-varying temperature at the MPMA level, materials able to convert the latter into electricity would be beneficial. Particularly well adapted materials to this end are pyroelectric elements able to directly link temperature changes into charge generation [13, 39]. While using pyroelectric elements into heat engines have been mentioned in a few studies [20], their actual implementation and investigation have barely been under consideration. Although a remarkable example was demonstrated by Ravindran et al. [21], the considered thermomechanical actuation (bistable mechanism triggered by gas expansion into a chamber) still requires a significant heat transfer from the thermal to the mechanical domain, hence deviating part of the energy from the main electrothermal energy conversion path. Hence, advantageous use of pyroelectric elements in the thermal behavior of the system is still an open question. With respect to the heat engine approaches devised here, Table 1 summarizes the key points of each possible heat engine technologies at small scale. Hence, it can be seen that one major bottleneck relies on the effective conversion of heat into electricity. Indeed, most of the reported implementations consider electromechanical energy conversion (through piezoelectric or electromagnetic coupling for instance), which therefore necessitates a supplementary conversion stage that is detrimental to the global thermal to electrical energy transfer efficiency. The only exception is the use of pyroelectric coupling in [21], but the propose solution still requires a mechanical movement that necessitates significant energy from the thermal source.

Hence, in order to address this issue, this paper proposes a MPMA-based heat engine using pyroelectric elements. The novelty behind the proposed concept, in addition to the combination of MPMAs (that feature magnetization gain as temperature increases) with pyroelectric energy conversion, consists in using direct heat transfer from heated MPMA to pyroelectric device (the latter being fixed), therefore enabling direct heat exchange and associated electrothermal conversion as well as facilitating MPMA cooling through this heat exchange for performance enhancement. Furthermore, the proposed concept allows a quite straightforward energy conversion path from thermal to electrical domain, with very little part used for mechanical actuation. The paper is organized as follows. Section 2 exposes the principles of the proposed concept along its modeling. The device is then experimentally implemented and devised in Section 3, with further design and optimization considerations given in Section 4. Finally, Section 5 concludes the paper, recalling the main findings of the study.

Ref.	Actuation	Harvesting	Advantages	Drawbacks
[20]	Shape Memory Alloys (SMAs)	Piezoelectric	• Integrable	• Multiple conversions in energy path (thermal/mechanical/electrical) • Thermal inertia of passive parts • Low electrothermal conversion efficiency
[22]	Shape Memory Alloys (SMAs)	Electromagnetic	• High power • Rotational	• Multiple conversions in energy path (thermal/mechanical/electrical) • Low electrothermal conversion efficiency • Difficult integration
[18]	Bimetallic strip	Piezoelectric	• Simple process	• Multiple conversions in energy path (thermal/mechanical/electrical) • Low electrothermal conversion efficiency
[21]	Gas expansion + bistable beam	Pyrolectric	• Direct thermal to electrical energy conversion	• Thermal inertia of passive parts • Significant thermal energy used to trigger mechanical snap-through • Low energy conversion efficient • Low frequency
[23]	Thermomagnetic (ferromagnetic)	Piezoelectric	• Integrable • High frequency	• Multiple conversions in energy path (thermal / mechanical / electrical) • May require high temperature magnets
[27–30]	Thermomagnetic (ferromagnetic SMA)	Electromagnetic (coil)	• Integrable • Frequency-up conversion	• Multiple conversions in energy path (thermal / mechanical / electrical) • Low electrothermal conversion efficiency • Requires high temperature magnets
[35]	Thermomagnetic (MPMA)	Electromagnetic (coil)	• Integrable • Frequency-up conversion	• Multiple conversions in energy path (thermal / mechanical / electrical) • Low electrothermal conversion efficiency

Table 1: Main small scale heat engine technologies and comparison.

2. Heat engine principles and theoretical developments

This section aims at exposing the concept and analysis of the proposed heat engine. More precisely, as a multiphysic system, thermal, mechanical and magnetic developments will be set up, along with the interfaces between these fields. Then, all aspects will be combined to allow the evaluation of the proposed device.

2.1. Device & operation principles

The fundamental concept of the proposed pyroelectric heat engine relies on the phase transition of Ni-Mn-Co-In MPMA that permits, in the considered temperature range, to enable magnetic behavior as the temperature increases thanks to the metamagnetic behavior. The device operations are illustrated in Figure 1. Starting from low temperature (1), the MPMA exhibits a non magnetic martensitic phase so that the flexural stiffness of the substrate cantilever beam ensures the contact of the MPMA with the hot source. As the MPMA is heated, it transits to the magnetic austenite phase, hence gaining magnetic properties, until its magnetic susceptibility is high enough to trigger sufficient magnetic attraction by the magnet with respect to the restoring force of the cantilever substrate. At this point, the MPMA therefore bends the beam, and comes in contact with the

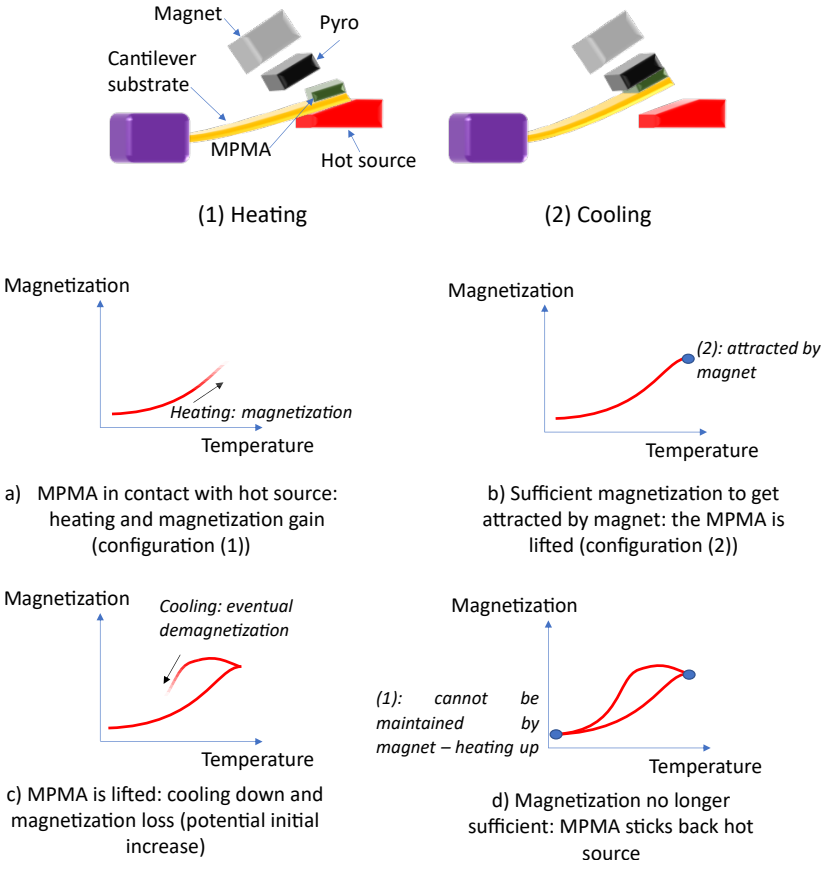

Figure 1: Heat engine concept.

pyroelectric element. The alloy therefore transmits part of its heat to the pyroelectric element, that converts it into electricity. Meanwhile, the MPMA cools down, reducing its magnetization and thus weakening the magnetic force from the magnet (2) until the flexural force becomes prevalent to bring the cantilever back to its initial state (1), initiating a new cycle.

Compared to previously developed heat engines (*e.g.*, [21, 23, 27, 29, 35]), the proposed concept has one or several of the following advantages:

1. The magnet is on the cold source side. This enables the use of conventional neodymium magnets, with no particular constraints on the temperature tolerance. Also, the device development is facilitated (less spacing and dimension issues).

2. The energy conversion material is separated from the actuation material. This therefore allows a simpler device development, but also helps in cooling down the MPMA faster, as the latter transfers part of its heat to the pyroelectric transducer.

3. Energy conversion path goes directly from the thermal domain to the electrical one, without significant part being used for mechanical excitation, accounting for a better energy thermo-electrical conversion of the source.

2.2. Analysis

Following the above exposed operation principles, this subsection aims at providing some theoretical considerations allowing the assessment of the device performance. The analysis will first consist in evaluating the thermal behavior and mechanical aspects separately (the latter also including magnetic interactions), that will be ultimately combined to derive the expectable harvesting abilities.

2.2.1. Thermal behavior

Assuming that the magnet is far away from the other parts of the device, it does not play any role in the thermal behavior. Furthermore, considering that MPMA and pyroelement thermal conduction coefficients are much higher than the other ones, their thermal resistances can be neglected and their temperatures can be considered as uniform (also due to their small thicknesses). The MPMA (and its substrate) being moveable, the air gaps on both sides (*i.e.*, between MPMA and hot source and between MPMA and pyroelectric element) exhibit varying thicknesses. Accordingly, the associated thermal lumped model as equivalent electrical circuit is given in Figure 2. R_{air} refers to the total thermal resistance of the air gap (both sides) that is fluctuating due to the movement of the MPMA beam. This movement is represent by the ratio x ($0 \leq x \leq 1$) of this total air gap distribution between both sides. Note that because of non-perfect contact (between MPMA beam and hot source or pyroelement), the respective minimal and maximal values of x may not be 0 and 1. R_{sub} and R_{sup} respectively represent the thermal conduction of MPMA substrate beam and superficial exchange (mainly convection) with ambient environment (pyroelectric substrate

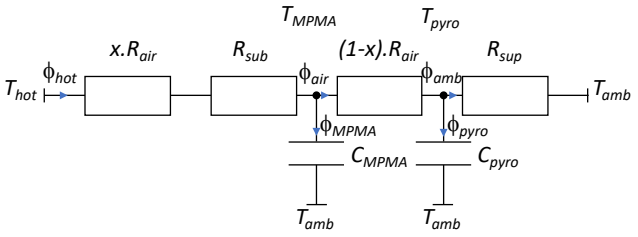

Figure 2: Heat engine thermal model.

conduction being considered negligible as well), while C_{MPMA} and C_{pyro} refer to the MPMA and pyroelement thermal capacitances, respectively. Finally, T_{hot} is the hot temperature, T_{amb} the cold (ambient) temperature and ϕ_{hot}, ϕ_{air}, ϕ_{amb}, ϕ_{MPMA} and ϕ_{pyro} the heat flux associated to each branch of the circuit.

Based on this model, the temperature difference and heat flux expressions follow:

$$\begin{cases} T_{hot} - T_{MPMA} = (xR_{air} + R_{sub})\,\phi_{hot} \\ T_{MPMA} - T_{pyro} = (1-x)R_{air}\phi_{air} \\ T_{pyro} - T_{amb} = R_{sup}\phi_{amb} \\ \phi_{hot} = \phi_{air} + \phi_{MPMA} \\ \phi_{air} = \phi_{amb} + \phi_{pyro} \\ \phi_{MPMA} = C_{MPMA}\frac{dT_{MPMA}}{dt} \\ \phi_{pyro} = C_{pyro}\frac{dT_{pyro}}{dt} \end{cases} \tag{1}$$

From Eq. (1) and considering the input temperature matrix $\mathbf{T} = [T_{hot}, T_{amb}]^t$ (^{t} denoting the transpose operator) and output temperature matrix $\mathbf{\Theta} = [T_{MPMA}, T_{pyro}]^t$, the following state-space equation can be derived:

$$\rho\mathbf{\Theta} + \tau\dot{\mathbf{\Theta}} = \mathbf{T} \tag{2}$$

where:

$$\begin{cases} \rho = \begin{bmatrix} \frac{R_{sub}+R_{air}}{(1-x)R_{air}} & -\frac{R_{sub}+xR_{air}}{(1-x)R_{air}} \\ -\frac{R_{sup}}{(1-x)R_{air}} & \frac{R_{sup}+(1-x)R_{air}}{(1-x)R_{air}} \end{bmatrix} \\ \tau = \begin{bmatrix} (R_{sub}+xR_{air})\,C_{MPMA} & 0 \\ 0 & R_{sup}C_{MPMA} \end{bmatrix} \end{cases} \tag{3}$$

From the above expression, it can be seen that the temperature variation is defined as a piecewise first order equation (the switching from heating to cooling being given by the value of the distance ratio x). Hence, it can be inferred that both hot and cold (ambient) temperatures have an impact on the dynamics of the system, due to the exponential shape of the temperature change.

2.2.2. Mechanical and magnetomechanical analysis

As a thermomechanical system, mechanical analysis of the heat engine is provided in this section. Globally speaking, the principle lies in the interaction between restoring force of the beam and magnetic force between the magnet and the MPMA. Considering that the MPMA is bonded at the end of a cantilever beam, the mechanical force F_{mech} can be obtained considering static bending stiffness K:

$$F_{mech} = Ku \tag{4}$$

where u is the tip displacement and K is given as:

$$K = 3\frac{EI}{l^3} \tag{5}$$

with E the elastic modulus, I the area moment of inertia ($I = (wh^3)/12$ with w the beam width and h its thickness in the case of a homogeneous rectangular beam) and l the beam length.

On the magnetic side, considering axisymmetric arrangement of the magnet, 2D problem (magnet and MPMA in the same plane) and thin and homogeneously magnetized MPMA leads to the following expression of the magnetic force $\mathbf{F_{mag}}$ on the MPMA ([40]):

$$\mathbf{F_{mag}} = V_{MPMA}\Big(\mathbf{M}(T_{MPMA}, \mathbf{B}).\nabla\Big)\mathbf{B} \tag{6}$$

where V_{MPMA} is the MPMA volume, $\mathbf{M}(T_{MPMA}, \mathbf{B})$ its magnetization vector and $\mathbf{B}$ the magnetic flux density vector applied to the material. Assuming that the low susceptibility of the MPMA does not significantly change the field lines generated by the magnet and magnetic linear response of the MPMA, its magnetization yields:

$$\mathbf{M}(T_{MPMA}, \mathbf{B}) = \frac{1}{\mu_0}\frac{\chi(T_{MPMA})}{1+\chi(T_{MPMA})}\mathbf{B} \tag{7}$$

with $\chi(T_{MPMA})$ the temperature-dependent MPMA magnetic susceptibility and $\mu_0 = 4\pi\times10^{-7}$ T.m.A^{-1} the vacuum permeability. Hence, in the device plane, the magnetic force turns to, in cylindrical coordinates ([40]):

$$\mathbf{F_{mag}}(r,z,T_{MPMA}) = \begin{bmatrix} F_r(r,z,T_{MPMA}) \\ F_z(r,z,T_{MPMA}) \\ F_\theta(r,z,T_{MPMA}) \end{bmatrix} = \frac{V_{MPMA}}{\mu_0}\frac{\chi(T_{MPMA})}{1+\chi(T_{MPMA})}\begin{bmatrix} B_r(r,z)\frac{\partial B_r(r,z)}{\partial r} + B_z(r,z)\frac{\partial B_z(r,z)}{\partial r} \\ B_r(r,z)\frac{\partial B_r(r,z)}{\partial z} + B_z(r,z)\frac{\partial B_z(r,z)}{\partial z} \\ 0 \end{bmatrix} \tag{8}$$

where F_r, F_z and F_θ are the respective radial, axial and azimuthal components of the force, and B_r and B_z the radial and axial components of the magnetic flux density, respectively. r and z denote the radial and axial distances, respectively. Finally, the effective force acting on the MPMA

beam can be obtained through the projection of $\mathbf{F_{mag}}$ on the displacement axis of the beam (*i.e.*, normal unitary vector $\mathbf{n}$):

$$F_{mag}(r, z, T_{MPMA}) = \mathbf{F_{mag}}(r, z, T_{MPMA}).\mathbf{n} \tag{9}$$

Combining the beam and magnetic forces further allows deriving the conditions for obtaining oscillations:

$$\begin{array}{ll} F_{mag}\left(r_{max}, z_{max}, T_{\ MPMA}|_{max}\right) > Ku_{min} & \text{(attraction by magnet)} \\ F_{mag}\left(r_{min}, z_{min}, T_{\ MPMA}|_{min}\right) < Ku_{max} & \text{(pulling back to hot source)} \end{array} \tag{10}$$

with r_{max} (*resp.* r_{min}) and z_{max} (*resp.* z_{min}) respectively denoting the radial and axial distances when the MPMA is far away from (*resp.* close to) the magnet[1], u_{min} and u_{max} the minimal and maximal beam deflection, and $T_{\ MPMA}|_{min}$ and $T_{\ MPMA}|_{max}$ the minimal and maximal MPMA temperature (obtained from Section 2.2.1).

2.2.3. Evaluation of generated power

The pyroelectric element is a ferroelectric element deriving from dielectric materials. From the constitutive equation of the direct effect pyroelectricity along polarization axis (considered to be the 3-axis):

$$D_3 = \epsilon_{33}^T E_3 + pT_{pyro} \tag{11}$$

where D and E are respectively the electric induction and electric fields, ϵ_{33}^T the permittivity at constant temperature and p the pyroelectric coefficient, the system-level equation is given as:

$$I = \alpha \dot{T}_{pyro} - C_0 \dot{V} \tag{12}$$

with I and V the outgoing current and voltage, respectively. α and C_0 are the current factor and clamped capacitance given as:

$$\left\{ \begin{array}{rcl} \alpha & = & -Ap \\ C_0 & = & \frac{\epsilon_{33}^T A}{e} \end{array} \right. \tag{13}$$

where A and e respectively denote the cross-sectional area and thickness of the material.

In the framework of the evaluation of energy conversion and harvesting abilities, a resistive load R_L is connected to the transducer. Accordingly, the governing equation yields in harmonic analysis, with ω the angular frequency:

$$\frac{V(\omega)}{R_L} = j\omega\alpha T_{pyro}(\omega) - j\omega C_0 V(\omega) \tag{14}$$

[1]Note that the global distance is considered so that r_{min} may be greater than r_{max}.

leading to the expression of the associated average power P (* denotes the complex conjugate):

$$P = \frac{1}{2}\frac{V(\omega)V^*(\omega)}{R_L} = \frac{1}{2}\frac{R_L\alpha^2\omega^2}{1+(R_L C_0\omega)^2}\left(\Delta T_{pyro}\right)^2 \tag{15}$$

with ΔT_{pyro} the temperature variation magnitude. Deriving and canceling Eq. (15) with respect to the load resistance shows that the optimum value of the latter is $(R_L)_{opt} = 1/(C_0\omega)$ giving the maximal power P_{max} as:

$$P_{max} = \frac{1}{4}\frac{\alpha^2}{C_0}\omega\left(\Delta T_{pyro}\right)^2 \tag{16}$$

3. Experimental validation

3.1. Experimental set-up and characterization

The experimental device and associated set-up is depicted in Figure 3. The harvester consisted of a polyimide (PI) cantilever beam of 14 mm in length, 2 mm in width and 25 μm in thickness. The MPMA material, consisting of a Nickel-Manganese-Indium-Cobalt compound ($Ni_{45}Co_5Mn_{36.6}In_{13.4}$), was glued at the end of the beam on a surface of 3×2 mm^2. The total thickness of the MPMA and glue is 200 μm. Manufacturer datasheet [41] shows that the PI elastic modulus varies from 2.5 GPa at 23 $^\circ$C to 2 GPa at 200 $^\circ$C. According to the device working conditions, a value of 2.1 GPa was selected, so that the bending stiffness was found to be 6 mN.m^{-1} using Eq. (5). Such a value was then confirmed by placing a small mass of paper at the end of the beam in horizontal configuration and measuring the difference in deflection produced by the paper weight. To ensure good contact between the PI/MPMA beam and heat source, as well as providing a bias restoring force, the beam was pre-bent to exhibit a 2 mm tip deflection. According to the flexibility of the polyimide substrate, its relatively limited displacement and good temperature resilience, no mechanical fatigue was neither expected nor experienced.

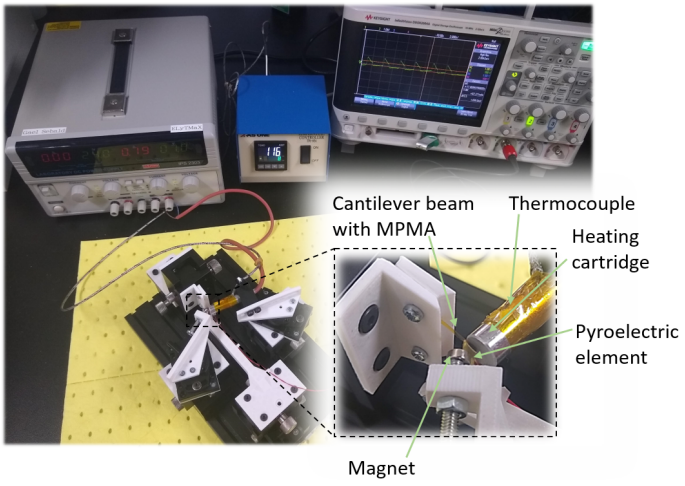

Figure 3: Experimental set-up.

A PTC heater (STEGO RCE 016) was used as hot source, with a thermocouple attached to it to monitor the temperature using a AS One TR-KN temperature controller. Note that an external laboratory power supply was used to provide electrical current to the heater, in order to efficiently control the maximal current not to damage the unit. The applied voltage and current were manually tuned to provide a hot temperature of approximately 115 $^\circ$C. These conditions may for instance reflect surface temperature of hot pipes, or temperature obtained through concentration of incoming solar energy, although concentrators may compromise the small-scale dimensions for the latter aspect. In practical application however where the working temperature range is fixed, design parameters such as ferromagnetic transition temperature should be tuned in order to comply with operating environment. Tuning this transition can be done for instance by modifying the composition of the MPMA.

On the other side, a 6 mm diameter, 2.2 mm thick neodymium magnet was placed, with a surface magnetic flux density measured as 0.2 T. As previously noted, the magnet is placed on the cold side (ambient temperature) thanks to the specific characteristics of the MPMA (magnetization gain with increasing temperature), allowing the use of conventional neodymium magnet. Finally, between the magnet and the PI/MPMA beam, a pyroelectric element was placed. This pyroelectric element was obtained by cutting a 5×5 mm^2 squared shape (active surface) into a commercial piezoelectric buzzer (Murata 7BB-20-3), with an active element thickness of 120 μm bonded onto a 100 μm thick brass substrate. For electrode soldering and clamping purposes, the total surface of the pyroelectric element (active and passive parts) is 4 times the active surface. Measured capacitance of the transducer was 2.25 nF, consistent with measured dimensions and typical PZT relative permittivity ($\geq$1000). The distance between pyroelement and heat source was determined to be 650 μm, while the pyroelement and the magnet center were separated by 3.1 mm.

From material characteristics and previous measurements, system parameters are given in Table 2. Thermal parameters (conductivity, superficial exchange coefficient) have been obtained from manufacturers' datasheets, yielding values reported in Table 3. The MPMA characteristics were obtained considering the alloy composition ratio. The total heat capacitance of the pyroelectric element comprised both PZT and brass.

3.2. Magnetic characterization

Prior to heat engine operations, magnetic characterizations and computations for both MPMA and magnet have been performed in order to derive the magnetic force.

3.2.1. Magnetic force exerted by the magnet

In the case of a cylindrical magnet of half radius a and half height b as considered in the present study, the expressions of the radial and axial components of the magnetic flux density (namely B_r and B_z, respectively) can be given from elliptic integrals as [52]:

Mechanical parameters	
Beam stiffness K	6 mN.m^{-1}
Thermal parameters	
Substrate thermal conduction resistance R_{sub}	26 K.W^{-1}
Total air thermal conduction resistance R_{air}	4300 K.W^{-1}
Thermal superficial exchange resistance R_{sup}	670 K.W^{-1}
MPMA thermal capacitance C_{MPMA}	4.2×10^{-3} J.K^{-1}
Pyroelectric element thermal capacitance C_{pyro}	40×10^{-3} J.K^{-1}
Air thermal resistance ratio when in contact with hot side x_{min}	0.05
Air thermal resistance ratio when in contact with pyro x_{max}	0.95
Electrothermal parameters	
Current factor α (pyroelectric coefficient of -570 μC.K^{-1}.m^{-2} - [42])	14×10^{-9} C.K^{-1}

Table 2: Experimental parameters.

Parameter	Value	Source
Substrate thermal conductivity	160 mW.m^{-1}.K^{-1}	[43]
Air thermal conductivity	25 mW.m^{-1}.K^{-1}	[44]
Thermal superficial transfer coefficient	15 W.m^{-2}.K^{-1}	[45]
MPMA volumetric heat capacity	3.5 MJ.m^{-3}.K^{-1}	[46–49], according to stoichiometric ratio
PZT volumetric heat capacity	2.7 MJ.m^{-3}.K^{-1}	[50]
Brass volumetric heat capacity	3.2 MJ.m^{-3}.K^{-1}	[51]

Table 3: Thermal material parameters.

$$\begin{cases} B_r &= B_r\Big[\alpha_+ C\left(k_+,1,1,-1\right) - \alpha_- C\left(k_-,1,1,-1\right)\Big] \\ B_z &= B_r \frac{a}{a+r}\Big[\beta_+ C\left(k_+,\gamma^2,1,\gamma\right) - \beta_- C\left(k_-,\gamma^2,1,\gamma\right)\Big] \end{cases} \tag{17}$$

where:

$$\begin{aligned} z_\pm &= z \pm b \\ \alpha_\pm &= \frac{a}{\sqrt{{z_\pm}^2+(r+a)^2}} \\ \beta_\pm &= \frac{z_\pm}{\sqrt{{z_\pm}^2+(r+a)^2}} \\ k_\pm &= \sqrt{\frac{{z_\pm}^2+(a-r)^2}{{z_\pm}^2+(a+r)^2}} \\ \gamma &= \frac{a-r}{a+r} \end{aligned} \tag{18}$$

and with C being the following generalized complete elliptic integral:

$$C(k,p,c,s) = \int_0^{\pi/2} \frac{c\cos^2\phi + s\sin^2\phi}{\left(\cos^2\phi + p\sin^2\phi\right)\sqrt{\cos^2\phi + k^2\sin^2\phi}} d\phi \tag{19}$$

From the computation of the magnetic flux density field, along with the related force expression given by Eq. (8), Figure 4 depicts the effect of the magnet in the experimental configuration. It can be shown that the MPMA is actually placed close to a position showing relatively sharp variation of the magnetic flux density, yielding relatively high flux density gradient and thus force. Meanwhile, the pre-bending of the beam by the PTC heater also offers a quite good alignment of the magnetic force streamlines with the normal direction of the MPMA, ensuring that most of the magnetic force is actually used for lifting the beam.

More precisely, it has been determined that the median angle φ between the magnetic force and MPMA surface varies from 10 ° (MPMA in contact with heater) to 40 ° (contact with pyroelement). Using the expression of the effective force acting on the MPMA given by Eq. (9), the median effective force density coefficient ψ (*i.e.*, force density removing the susceptibility-dependent term and adding angle effect):

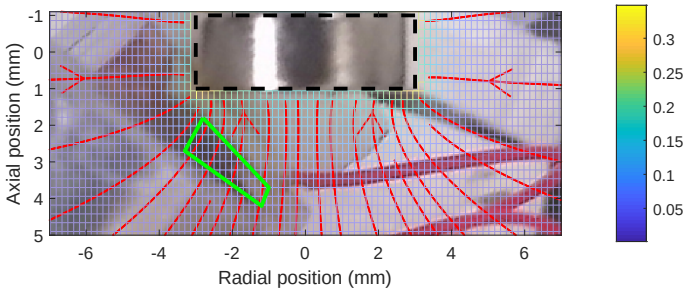

Figure 4: Magnetic effects of the permanent magnet: grid represent magnetic flux density intensity and streamlines the force. Colorbar refers to the magnetic flux density magnitude. Magnet is depicted within thick dashed black lines and MPMA moving area is delimited in thick plain green lines.

$$\psi = \cos(\phi)\sqrt{\left(B_r(r,z)\frac{\partial B_r(r,z)}{\partial r} + B_z(r,z)\frac{\partial B_z(r,z)}{\partial r}\right)^2 + \left(B_r(r,z)\frac{\partial B_r(r,z)}{\partial z} + B_z(r,z)\frac{\partial B_z(r,z)}{\partial z}\right)^2} \tag{20}$$

is depicted in Figure 5 for the MPMA-magnet distance range in the considered experiment (3.3-3.9 mm). Associated quadratic fit gave the following approximation (with d the distance between center of MPMA and magnet center, in meter):

$$\psi \approx -2.2 \times 10^5 d^2 + 840d + 0.76 \tag{21}$$

leading to the force expression:

$$F_{mag}(d,T) = \frac{V_{MPMA}}{\mu_0}\frac{\chi(T_{MPMA})}{1+\chi(T_{MPMA})}\psi \approx \frac{V_{MPMA}}{\mu_0}\frac{\chi(T_{MPMA})}{1+\chi(T_{MPMA})}\left(-2.2 \times 10^5 d^2 + 840d + 0.78\right) \tag{22}$$

3.2.2. Magnetic response of MPMA

In order to evaluate the low-field susceptibility, a MPMA sample with same composition as the one used in the experiment but in the shape of film was characterized using SQUID magnetometer (MPMS2, Quantum Design, Inc.). External flux density was fixed to 50 mT. Local heating on the sample allowed to vary the temperature up to 125 °C. Heating and cooling cycles were considered, leading to results depicted in Figure 6. Results show a significant dependence of the magnetic susceptibility upon the temperature, with a sharp increase arround 100 °C in heating stage. A hysteretic behavior is also observed when considering major temperature cycles.

3.3. Experimental results

Using the exposed configuration, the heat engine shows oscillations with a mean period of approximately 3 s. Thermal imaging equipment (Optris™Xi 400 thermographic camera) allowed extracting the temperature map in the zone where MPMA moves (the MPMA temperature being

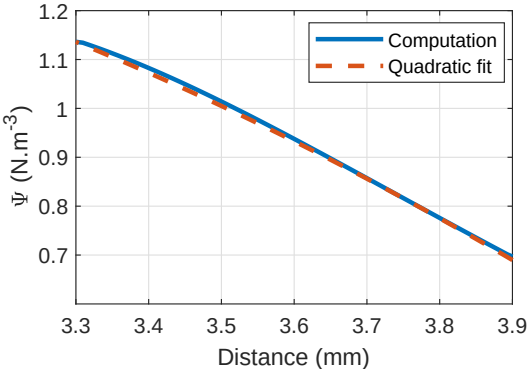

Figure 5: Force density coefficient evolution with the distance and quadratic fit.

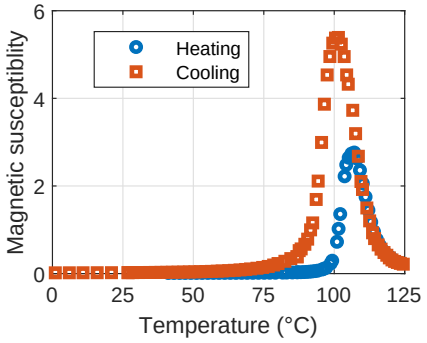

Figure 6: Magnetic characterization of MPMA.

considered as the maximum temperature in the zone). Results are depicted in Figure 7, showing a MPMA temperature variation from 55 ° C to 81 ° C. Note that no particular coating was applied at the end of the heater (middle part is covered by polyimide tape) and on the magnet, yielding inaccurate temperature reading on these particular elements due to low emissivity. The time-dependent variation of the temperature was further confirmed by computing the difference of thermal image between hot and cold cases (Figure 8). Finally, temperature reading close to the MPMA working area indicated a pyroelectric element average temperature around 40 ° C.

Due to the small capacitance value and low frequency, the output impedance of the pyroelectric element is 210 MΩ. Hence, directly connecting the transducer to the oscilloscope (1 MΩ input impedance) yields electrical condition close to short circuit. Therefore obtained voltage is an image of the current, depicted in Figure 9, obtained in steady-state operations after heating up of the PTC heater and thermalization of the pyroelement, which last a few cycles[2]. Hence, with an average oscillation period of 3 seconds and a measurement time range of 50 seconds, approximately 16 oscillations are observed, which is considered sufficient to analyze the device operations in steady-state. From the integration of this current (yielding generated electric charges) and division by the cross-sectional area and pyroelectric coefficient, the temperature variation around the bias temperature can be obtained, as depicted in Figure 10. It can be shown that the pyroelectric temperature does not varies significantly (RMS value: 0.31 ° C), possibly due to an imperfect thermal contact between the MPMA and the pyroelement, but also because of the larger thermal capacitance of the pyroelectric element (and its substrate) compared to the MPMA (notably due to larger dimensions of the pyroelectric transducer). Part of the exchanged heat also flows to the ambient environment through superficial exchanges. This difference however highlights the possibility of separately tuning the MPMA operations for actuation and energy harvesting process enabled by the pyroelectric element, therefore allowing a simpler device development.

[2]While it is not possible to experimentally observe the sole pyroelement thermalization effect (due to heating up of the PTC cartridge), simulations indicate a slightly larger response of the pyroelectric element in the transient stage.

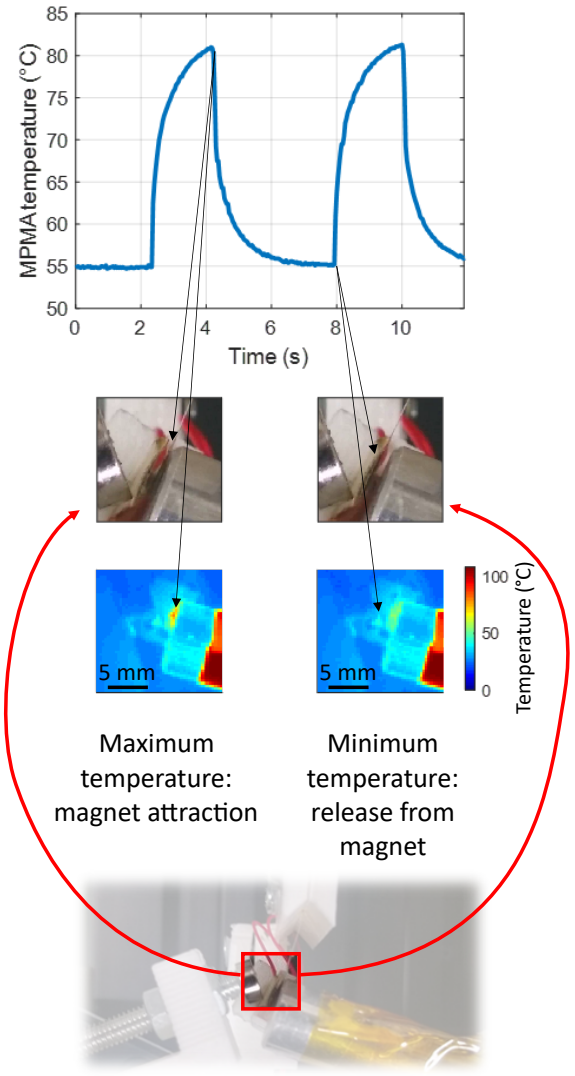

Figure 7: Temperature response and associated photograph and thermal map.

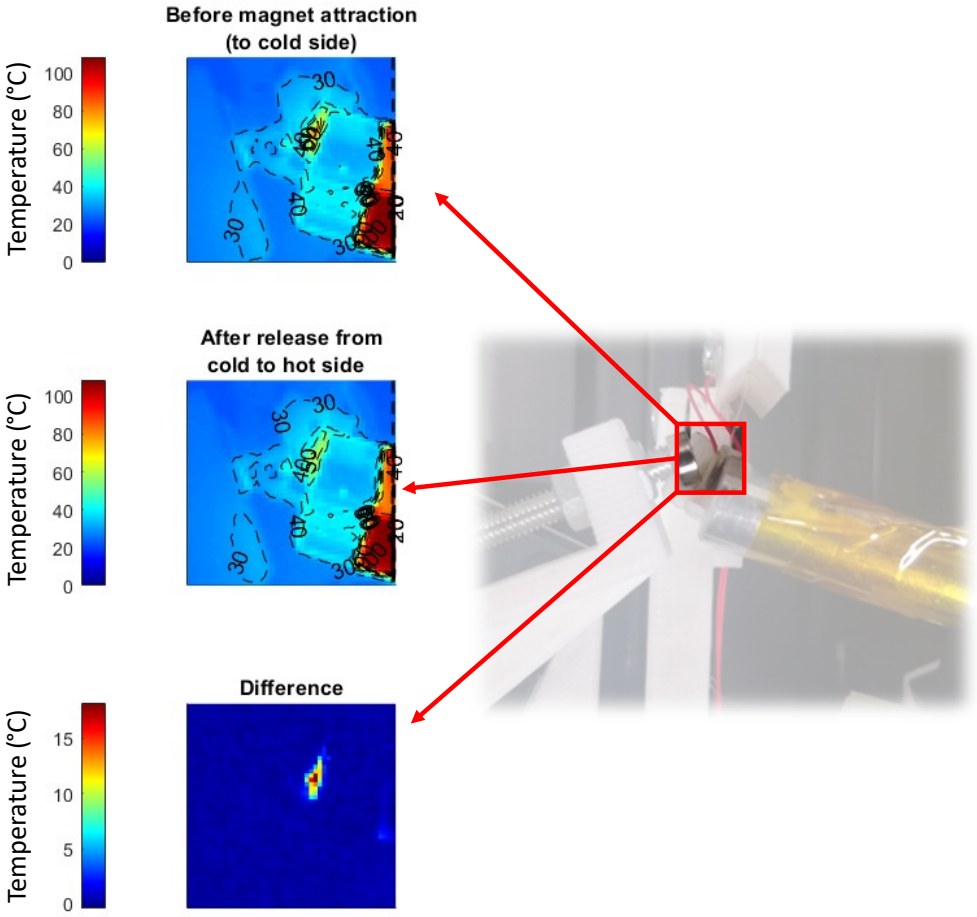

Figure 8: Thermal map and difference.

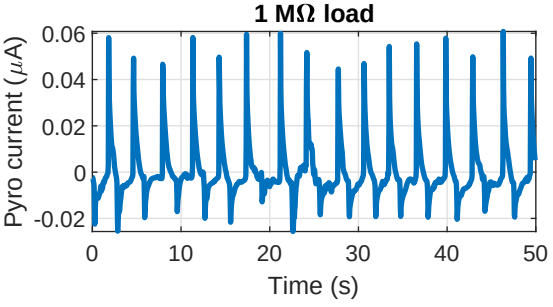

Figure 9: Pyroelectric transducer current with a load of 1 MΩ.

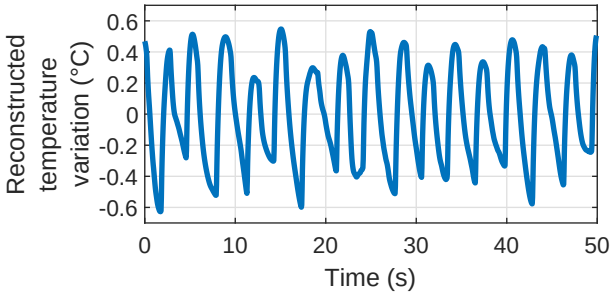

Figure 10: Reconstructed pyroelectric transducer temperature variation.

Output voltage of the pyroelectric element on a 100:1 probe with an input impedance of 100 MΩ is shown in Figure 11. From these results, average power density was found to be 4.83 μW.cm^{-3}. When taking into account the cantilever beam and the transducer (active part), the power density is 1.17 μW.cm^{-3}. Normalizing these results to the energy generation per cycle (as scaling the device up or down would certainly change the oscillation frequency without changing the transition dynamics too much), this yields a value of 14.32 μJ.cm^{-3}.cyle^{-1}. The peak power density was estimated to 22 μW.cm^{-3} with respect to the MPMA volume, which is less than previous similar devices using MPMA and electromagnetic conversion through a microcoil operating at high frequency through frequency-up conversion mechanisms [35]. However, previously exposed average power densities, reflecting the ability of actually supplying energy in a continuous way, show increases by factors from 3 (power density with respect to MPMA) to 26.7 (energy density per cycle) compared to the same devices. Such an enhancement is actually enabled not only by the better energy conversion abilities of pyroelectric materials with respect to microcoil at small scale (as the pyroelectric element allows directly converting heat energy into electricity as previously noted, without the need of going through mechanical domain), but also thanks to the principle of heat transfer from the MPMA to the pyroelectric element. Yet, there is lot of room for optimization in terms of material, system and their co-design, as demonstrated by other heat engines exposed in the literature (for example, it is estimated in [35], using a very similar alloy, that orders of magnitude can be gained, notably by material design and oscillating structure optimization). In

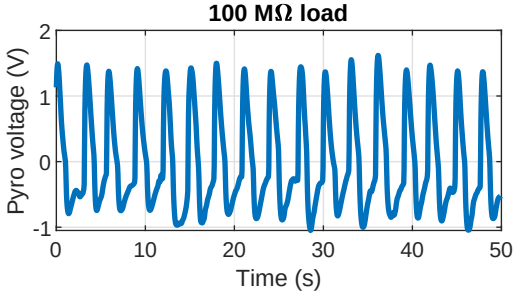

Figure 11: Pyroelectric transducer voltage with a load of 100 MΩ.

this view, Section 4 will expose possible routes for enhancing the device performance.

Assuming that the device operation can be approximated by its harmonic response and following Eq. (15), the theoretical power is found to be 14×10^{-11} W and 7×10^{-9} W, respectively for 1 MΩ and 100 MΩ loads. Such values are in quite good agreement with experimentally measured powers, equal to 8.7×10^{-11} W and 5.8×10^{-9} W for 1 MΩ and 100 MΩ loads respectively. At the considered frequency, the optimal load being equal to 210 MΩ, a further gain of 30% can be expected by better load matching.

3.4. Comparison with theoretical predictions and discussion

Using previously identified parameters, the model exposed in Section 2.2 has been numerically implemented for assessing its performance in reflecting experimental data, allowing further optimization works. Prior to this evaluation, MPMA susceptibility has been investigated in the temperature range of interest (40-90 °C). Compared to results shown in Figure 6, the heat engine working temperature range does not correspond to the temperature range where the MPMA features highest susceptibility. While this prevents from benefiting from high susceptibility variations, this has the advantage of not requiring significant energy conversion from thermal to mechanical domains, therefore focusing the energy path on thermal aspect for more efficient pyroelectric element conversion. In addition, this allows drastically reducing the hysteretic behavior of the thermally-induced MPMA magnetic response as only minor cycles are involved. Finally, this permits a significant reduction of the structural stress due to phase transition, and thus limits potential ageing that would affect the material characteristics over time.

With respect to these observations, only susceptibility in heating conditions are under consideration. Furthermore, for an easier implementation of the numerical resolution, the MPMA magnetic response has been fitted using a sigmoid function following an Ising-like model relating well phase transitions [53]:

$$\chi(T_{MPMA}) = \frac{\chi_{max} - \chi_0}{2} \left[1 + \frac{2}{\pi} \arctan\left(\frac{T_{MPMA} - T_c}{\Upsilon} \right) \right] + \chi_0 \tag{23}$$

where χ_{max} and χ_0 are respectively the maximal and minimal (low temperature) susceptibilities, T_C the half-transition temperature and Υ the slope coefficient. Using $\chi_{max} = 58 \times 10^{-3}$, $\chi_0 = 12 \times 10^{-3}$, $T_c = 89$ °C and $\Upsilon = 6.25$ °C yields the results depicted in Figure 12, showing a good match between experimental points and fitted curved in the temperature range of interest.

Implementing this equation and identified parameters within the previous model, as well as considering hot side and cold side temperatures as 115 and 25 °C respectively, leads to the results shown in Figure 13. Globally, simulation shows good agreement with experimental direct and indirect measurements. Minor discrepancies, notably on the system's dynamics, can be attributed to the slightly different magnetic response of the glued MPMA compared to the film sample used for characterization (although same raw material) as well as the glue effect. Another important

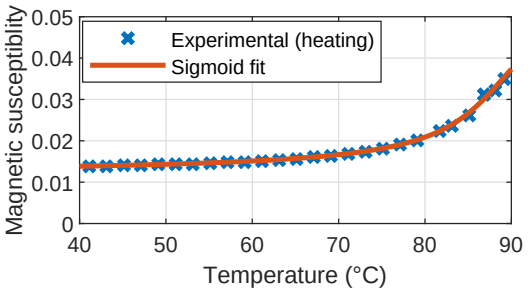

Figure 12: Susceptibility in temperature range of interest and fitted curve.

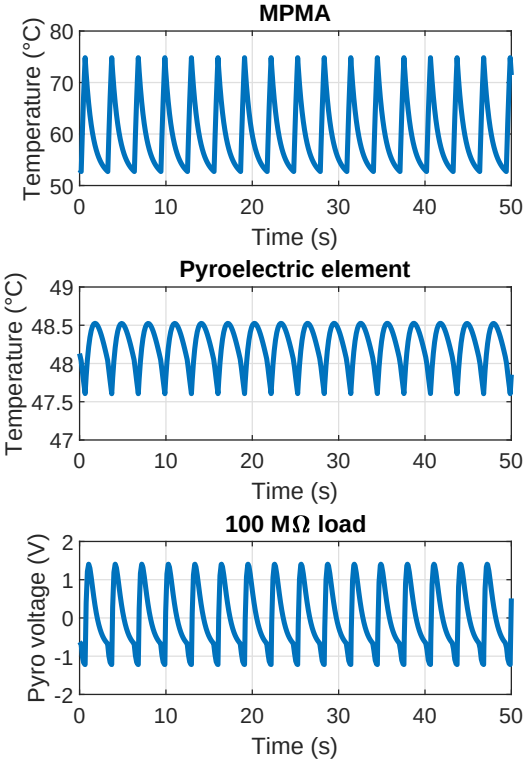

Figure 13: Numerical results using theoretical model.

aspect is the fact that the MPMA has been characterized considering low-field response (external flux density of 50 mT), while it experiences higher fields in experiments, especially when in close distance to the magnet. Also, the maximal temperature reached by the MPMA in simulations (75 °C) is less than experiments (81 °C). Again, this can be explained by the slight difference in magnetic response of the MPMA compared to characterization, as well as a possible nonlinear mechanical behavior of the beam. Minimal temperatures, corresponding to higher beam restoring force leading to contact to hot source, are however similar (55 °C in experiments vs. 52 °C in simulation).

Still, simulation gives results highly consistent with experiments. In particular, peak-to-peak voltage on a 100 MΩ load are in good agreement (∼2.2 V in experiments and 2.6 V in simulations) as well as its RMS value (0.76 V in experiments in 0.79 V in simulation). While slightly higher in simulation than expected from experimental coarse evaluation, pyroelectric mean temperature value was confirmed in simulation, with a value of 48.2 °C. Its RMS variation was found to be 0.27 °C in simulation, which is similar to the value of 0.31 °C in experiments.

4. Optimization considerations

Based on the previously established numerical model, this Section proposes analyzing the effect of some key device parameters. In addition, ferroelectric materials enabling the use of extracted energy magnification interfaces [54, 55] that have also be shown to be adapted to pyroelectric devices [39], effects of the latter on the energy conversion abilities will be devised as well.

4.1. Device configuration

This part aims at investigating the thermally-induced mechanical oscillations in the reported heat engine, and successive heat transfers from the hot source to the MPMA and then from the MPMA to the pyroelement. Hence, because of the coupling between the thermal, magnetic and mechanical parts, associated parameters will be under consideration, and more particularly :

- for the thermal aspect: based on the lumped model shown in Figure 2, one critical aspect is to ensure good contact between the MPMA and hot side during heating process and between MPMA and pyroelectric element during cooling. This is represented by the distance ratio x.
- for the thermomagnetic aspect: mechanical movement of the device finds its root in the varying magnetic properties (magnetic susceptibility) of the MPMA with the temperature. One key parameter of this dependence lies in the ferromagnetic transition temperature T_C.
- for the mechanical aspect: oscillations of the heat engine arise from the balance of the magnetic force exerted by the magnet on the MPMA and the restoring force of the beam. While the former is related to the thermomagnetic properties described above, the latter is mainly dependent on the beam stiffness K.

Due to system design constraints (surface flatness and parallelism, glue layer...), contacts between MPMA and hot source and between MPMA and pyroelectric element is not perfect. This has been previously modeled as distance ratio x, where the minimal value corresponds to the contact with the hot source ($x_{min} = 0$ means perfect contact with hot source) and the maximal one to the contact with the pyroelectric element ($x_{max} = 1$ means perfect contact). Varying these values while keeping all the other ones as previous yields results depicted in Figure 14. For both x_{min} and x_{max}, the other extreme limit (in addition to 1 for x_{max} and 0 for x_{min}) has been set to 0.5, corresponding to the middle distance between the pyroelectric element and the hot source. While predictably the pyroelectric RMS voltage increases with the increase of the maximal distance ratio (better contact with the pyroelectric element), with no operation below $x_{max} \approx 0.6$, the minimal ratio is surprisingly rather flat, even showing an optimal value around 0.25. Such an effect can however be attributed to a higher pre-bending of the beam, therefore requiring higher magnetic force and thus MPMA susceptibility. Achieving this higher value requiring higher temperature, more heat is stored in the MPMA and then released to the pyroelectric element (which thus experiences larger temperature swing without significant increase of the mean temperature as cooling time is longer), yielding higher power in spite of lower frequency. Such an observation however assumes linear operations of the pyroelectric element, which is nevertheless valid in the considered temperature range.

Another aspect under consideration is the MPMA susceptibility dependence with the temperature and associated magnetic force. While in experiments, temperature range corresponding to low susceptibility and susceptibility variation was selected, one may consider to use temperature ranges where the susceptibility variation is the highest. This also requires properly tailoring the beam stiffness value or the magnetic force function of the magnet to ensure that magnetic and mechanical forces balance arises in the high magnetic susceptibility variation range. When considering the former way along with a change in transition temperature T_c, numerically obtained RMS

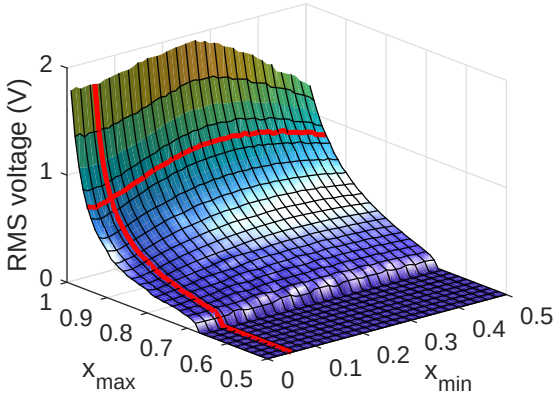

Figure 14: Simulation results for varying minimal and maximal distance ratios (thick red lines represent current experimental conditions for each variable; the crossing point thus being the experimental configuration).

voltage are displayed in Figure 15.

These results highlight that working close to the transition temperature, where susceptibility slope is the highest, actually yields non-optimal operations. For example, Figure 15 shows that for a fixed transition temperature, the optimal stiffness is the lowest one that ensures device operation, which corresponds to the lowest possible temperature range (typically much below the transition one). When considering fixed stiffness, performance increases when transition temperature moves towards high values, hence out of range of the working temperature range. It can be noted that for the specific material used in experiment, the chosen stiffness yields a working point close to optimal operations.

Such observations actually arise from the energy conversion principles of the proposed heat engine which relies on heat transfer, contrary to conventional implementations that consist in converting thermal energy into mechanical motions prior to electrical conversion through electromagnetic [27, 29, 35] or piezoelectric [23] effects. In the present case, mechanical motion is solely used for MPMA movement to trigger either heat exchange from the hot source to the MPMA (heat storage) or from the MPMA to the pyroelectric element (heat release), the latter mechanism initiating thermal to electrical energy conversion. Hence, enough heat should be stored when the MPMA is in contact with the hot source, hence necessitating a relatively wide temperature variation range. Thus, a slowly varying magnetic susceptibility is beneficial to this end, although limiting vibration frequency at the benefit of temperature magnitude. However, minimal values for maximal and minimal magnetization levels are still mandatory in order to allow the vibration of the structure. This aspect is shown in Figure 15 through the non-operating (zero voltage) zone, as well as the decrease of the required stiffness, already quite low, to go to the operating zone as the transition temperature increases. Also, and while not taken into account in the present simulation, hysteresis in the temperature-dependent susceptibility may further limit the interest in exploiting sharp susceptibility variation in the proposed device. Even reduced, hysteresis may

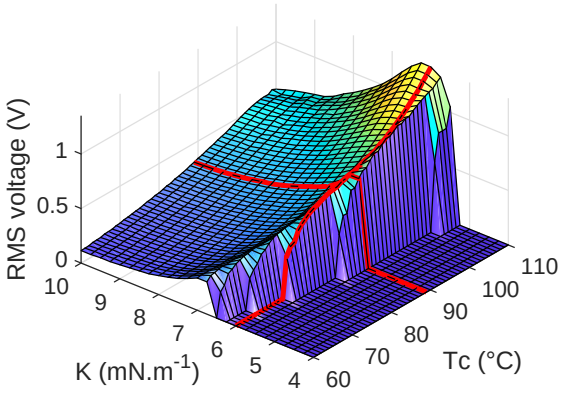

Figure 15: Simulation results for varying transition temperature and beam stiffness (thick red lines represent current experimental conditions for each variable; the crossing point thus being the experimental configuration).

still be present in considered minor loops, and should also be reduced as much as possible. These observations and conclusions are also of prior importance when designing the device for a specific application. Indeed, working temperatures are fixed by the considered application (heated pipe, electronic component such as processor...), and the materials and device characteristics have to match this operating environment. Hence, transition temperature of the MPMA should be selected accordingly to ensure good operations of the heat engine. In that sense, the property of the proposed device where the mechanical oscillations are not part of the main energy transfer path yields another interesting aspect of the proposed device. Indeed, the fact that transition temperature should be higher than actually operating temperature range allows simpler material and device development.

4.2. Electrical interface

Thanks to the dielectric nature of pyroelectric elements, nonlinear treatments of its output voltage allowing energy conversion enhancement may be considered. In particular, synchronized switch techniques have shown particular potentials in magnifying power output of piezoelectric and pyroelectric microgenerators [39]. Among such techniques, the so-called *Synchronous Electric Charges Extraction* (SECE) provides not only a power gain (up to 4 compared to standard DC case), but also features a load independence feature that is attractive in many practical applications [56], and is even more beneficial here due to the high value of optimal impedance due to low frequency oscillations. The underlying principles of the SECE consist in extracting all of the electrical charges, or equivalently electrostatic energy, available on the pyroelectric element when its voltage reaches an extremum value.

Hence, based on open-circuit voltage waveforms extracted from charge generation derived from experimentally measured short-circuit current, it is possible to investigate the possible benefit of the SECE interface when applied to the proposed device. Specifically, generated charges were obtained by integrating the short-circuit current. Then, the open-circuit voltage was derived by dividing electrical charges by the capacitance value. Finally, time integration of this voltage, that is reset on each extremum value, has been computed. Note that due to voltage continuity in such a dielectric medium, this reset is equivalent to changes in initial voltage condition. At each voltage cancellation, extracted energy E_i was estimated by:

$$E_i = \frac{1}{2} C_0 {V_i}^2 \tag{24}$$

with V_i referring to the extremal voltage just before cancellation.

When doing so, the obtained voltages and energy are given in Figure 16. Results indicate a potential average power using such an approach that is 3.6 times higher than in the experimental case that considered pure resistive load. Even taking into account a 75% efficiency between extracted energy and actual harvested one [56], the SECE interface still allows a gain of 2.7 compared

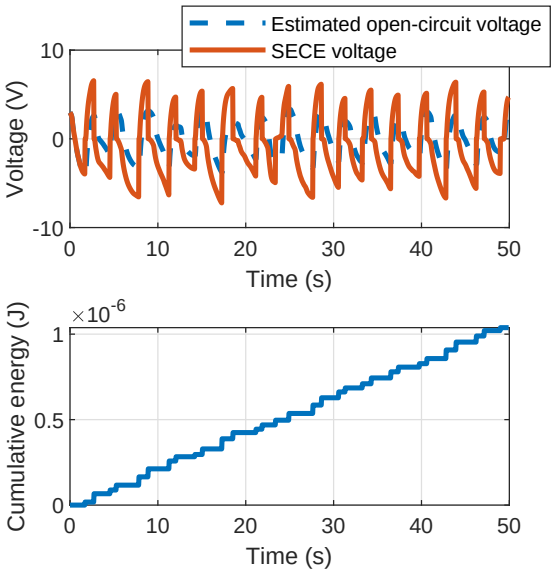

Figure 16: Estimation of open-circuit and SECE voltages and extracted energy using SECE derived from experimental short-circuit current.

to resistive case, corresponding to power densities of 13 μW.cm^{-3} with respect to MPMA volume and 3.15 μW.cm^{-3} when also taking into account beam and pyroelement volumes.

Hence, from the readily available harvester devised in this study, it can be shown that 1 μJ can be harvested within 50 s. While this energy appears to be very low, this would for example permit measurement and transmission every 6 hours considering STM300 module from Enocean ([57])[3]. However, circuit leakage and losses have not been taken into account in this calculation, and would require optimization of the harvester (as previously discussed) or upscaling ([30]) in order to provide more useable energy levels.

5. Conclusion

As an alternative to conventional thermoelectric modules for small scale thermal energy harvesting from temperature gradient, this study proposed a heat engine based on a MultiPhysic Memory Alloy (MPMA), that shows a reverse martensitic-austenite phase transition allowing a gain in magnetization with temperature, combined with pyroelectric element for thermal to electrical energy conversion. The reported concept proposes a new paradigm compared to most of conventional heat engines reported in the literature that rely on thermo-magneto-mechanical conversion (although mechanical medium is still used for displacement). Specifically, the use of a pyroelectric element permits a direct heat transfer from the MPMA and requires minor energy for mechanical medium. Mechanical movement is still implemented for moving back and forth from the hot source to the

[3]Assuming 3.3 V supply voltage, with respective consumption of 30 μA.s and 100 μA.s for each sensing and transmission cycle.

pyroelectric element (using a small fraction of the thermal energy that is converted into mechanical one), but is not used in the main energy flow for harvesting purposes, that directly goes from the thermal source to the electrical one thanks to the direct heat transfer from the MPMA to the pyroelectric element. In addition, the use of the pyroelectric element, capturing heat gained by the MPMA during heating stage, allows a faster cooling of the alloys, thus yielding an increased frequency.

Compared to similar devices using comparable metamagnetic Heusler alloy, experiments showed gains in terms of power densities by factors from 3 to 10 (according to the considered volume) and in terms of energy density per cycle by a factor of 26.7 (considering MPMA, beam and active part of transducer - *i.e.*, pyroelectric element). Preliminary investigations of optimization potentials showed that this power density can besides be further increased, through material and system optimization, or by appropriate electrical interfaces; the latter potentially providing an additional gain close to a factor of 3. Finally, the proposed concept can also be adapted to any heat engine using ferromagnetic materials or ferromagnetic Shape Memory Alloys, as the pyroelectric element could be placed on the hot side (only temperature variations are of consideration when it comes to pyroelectric energy conversion). Hence, the exposed method can also be adapted to high-performance heat engines using for instance Ni-Mn-Ga compounds, even possibly combining electromechanical (electromagnetic or piezoelectric effects) and electrothermal (pyroelectric coupling) conversion effects. By properly shaping the energy conversion routes (electrothermal - as in this study - or thermoelectromechanical) as well as thermal paths within the system, this would therefore provide means of small-scale energy harvesting devices with better performance than conventional thermoelectric modules. In that view, an interesting aspect would be the investigation of materials and devices dimensions that can yield benefits from up-scaling. Also, the experimental development of proper electrical interfaces, preliminary investigated here, is a complementary route for enhancing the global device performance. Finally, further works may also target the development of a complete demonstrator powering an autonomous sensor using the proposed concept.

Declaration of Competing Interest

The authors declared that there is no conflict of interest.

Acknowledgements

M. Lallart, L. Yan and H. Miki gratefully acknowledge the support of JSPS through invitational fellowship grant number L19530 and postdoctoral fellowship grant number PE19727. M. Lallart is also grateful to INSA-Lyon for its support through the CRCT program.

This work has been partly performed in the framework of the TATAMI project funded under the Collaborative Research Project of Lyon Center, IFS, Tohoku University (project code J20Ly05) and supported by IFS Lyon Center and ELyT Global IRN (projects TATAMI and MISTRAL).

References

[1] V. Knap, D.-I. Stroe, M. Swierczynski, R. Teodorescu and E. Schaltz, "Investigation of the Self-Discharge Behavior of Lithium-Sulfur Batteries", *J. Electrochem. Soc.*, Vol. 163 (6), A911-A916, 2016.

[2] J. VanZwol, "Designing battery packs for thermal extremes", *Power Electronics Technology*, July 2006, pp. 4045, 2006.

[3] D. Maurya, P. Kumar, S. Khaleghian, R. Sriramdas, M. G. Kang, R. A. Kishore et al., "Energy harvesting and strain sensing in smart tire for next generation autonomous vehicles" *Applied Energy*, Vol. 232, pp. 312–322, 2018.

[4] J. W. Matiko, N. J. Grabham, S. P. Beeby and M. J. Tudor, "Review of the application of energy harvesting in buildings", *Meas. Sci. Technol.*, Vol. 25, #012002, 2014.

[5] E. Romero, R. O. Warrington and M. R. Neuman, "Energy scavenging sources for biomedical sensors", *Physiol. Meas.*, Vol. 30, pp. R35–R62, 2009.

[6] F. K. Shaikh and S. Zeadally, "Energy harvesting in wireless sensor networks: A comprehensive review", *Ren. Sust. Energy Rev.*, Vol. 55, pp. 1041–1054, 2016.

[7] N. S. Hudak and G. G. Amatucci, "Small-scale energy harvesting through thermoelectric, vibration, and radiofrequency power conversion", *J. Appl. Phys.*, Vol. 103, # 101301, 2008.

[8] K. V. Selvan and M. S. Mohamed Ali, "Micro-scale energy harvesting devices: Review of methodological performances in the last decade", *Ren. Sust. Energy Rev.*, Vol. 54, pp. 1035–1047, 2016.

[9] R. A. Kishore and S. Priya, "A Review on Low-Grade Thermal Energy Harvesting: Materials, Methods and Devices", *Materials*, Vol. 11(8), #1433, 2018.

[10] F. J. DiSalvo, "Thermoelectric cooling and power generation", *Science*, Vol. 285, pp. 703–6, 1999.

[11] D. Enescu, "Thermoelectric Energy Harvesting: Basic Principles and Applications", in Green Energy Advances, D. Enescu Ed., IntechOpen, 2019. DOI: 10.5772/intechopen.83495. ISBN: 978-1-78984-200-5

[12] T. J. Seebeck, "Magnetische polarisation der metalle und erze durch temperatur-differenz", *Abhandlungen der Königlichen Akademie der Wissenschaften zu Berlin*, pp. 265–373, 1825.

[13] G. Sebald, D. Guyomar and A. Agbossou, "On thermoelectric and pyroelectric energy harvesting", *Smart Mater. Struct.*, Vol. 18, #125006, 2009.

[14] TE-CORE ThermoHarvesting Power Module Featuring ThermoGenerator-in-Package TGP-651 Preliminary Datasheet, http://www.micropelt.com/fileadmin/user_upload/_PDF_TE-CORE.pdf *(last viewed: 08/05/2020)*.

[15] Zeeshan, B. K. Panigrahi, R. Ahmed, M. U. Mehmood, J. C. Park, Y. Kim et al., "Operation of a low-temperature differential heat engine for power generation via hybrid nanogenerators ", *Applied Energy*, Vol. 285, #116385, 2021.

[16] X. Tong, S. Liu, J. Yan, O. A. Broesicke, Y. Chen and J. Crittenden, "Thermolytic osmotic heat engine for low-grade heat harvesting: Thermodynamic investigation and potential application exploration", *Applied Energy*, Vol. 259, #114192, 2020.

[17] A. Meir, A. Offner and G. Z. Ramon, "Low-temperature energy conversion using a phase-change acoustic heat engine", *Applied Energy*, Vol. 231, pp. 372-379, 2018.

[18] O. Puscasu, S. Monfray, J. Boughaleb, P.-J. Cottinet, D. Rapisarda, E. Rouvière et al., "Flexible bimetal and piezoelectric based thermal to electrical energy converters", *Sens. Act. A: Phys.*, Vol. 214, pp. 7-14, 2014.

[19] T. Huesgen, J. Ruhhammer, G. Biancuzzi and P. Woias, "Detailed study of a micro heat engine for thermal energy harvesting", *J. Micromech. Microeng.*, Vol. 20, #104004, 2010.

[20] H. H. S. Chang and Z. Huang, "Laminate composites with enhanced pyroelectric effects for energy harvesting", *Smart Mater. Struct.*, Vol. 19, #065018, 2010.

[21] S. K. T. Ravindran, T. Huesgen, M. Kroener and P. Woias, "A self-sustaining micro thermomechanic-pyroelectric generator", *Appl. Phys. Lett.*, vol. 99(10), #104102, 2011.

[22] D. Avirovik, R. A. Kishore, D. Vuckovic and S. Priya, "Miniature Shape Memory Alloy Heat Engine for Powering Wireless Sensor Nodes", *Energy Harvesting Syst.*, Vol. 1(1-2), pp. 13–18, 2014.

[23] M. Ujihara, G. P. Carman and D. G. Lee, "Thermal energy harvesting device using ferromagnetic materials", *Appl. Phys. Lett.*, Vol. 91, #093508, 2007.

[24] N. Tesla, "Thermo-Magnetic Motor", *US Patent 396121*, 1889.

[25] N. Tesla, "Pyromagneto-Electric Generator", *US Patent 428057*, 1890.

[26] F. Brailsford, "Theory of a ferromagnetic heat engine", *Electronics and Power*, Vol. 111(9), pp. 314 - 315, 1964.

[27] V. Srivastava, Y. Song , K. Bhatti and R. D. James, "The Direct Conversion of Heat to Electricity Using Multiferroic Alloys", *Adv. Energy Mater.*, Vol. 1, pp. 97–104, 2011.

[28] M. Kohl, M. Gueltig and F. Wendler, "Coupled Simulation of Thermomagnetic Energy Generation Based on NiMnGa Heusler Alloy Films", *Shap. Mem. Superelasticity*, Vol. 4, pp. 242–255, 2018.

[29] M. Gueltig, F. Wendler, H. Ossmer, M. Ohtsuka, H. Miki, T. Takagi et al., "High-Performance Thermomagnetic Generators Based on Heusler Alloy Films", *Adv. Energy Mater.*, Vol. 7, #1601879, 2017.

[30] J. Joseph, M. Ohtsuka, H. Miki and M. Kohl, "Upscaling of Thermomagnetic Generators Based on Heusler Alloy Films", *Joule*, Vol. 4, pp. 2718-2732, 2020.

[31] https://www.supermagnete.fr/eng/physical-magnet-data (last viewed: 18/12/2020).

[32] C. C. Pavel, R. Lacal-Arántegui, A. Marmier, D. Schüler, E. Tzimas, M. Buchert et al., "Substitution strategies for reducing the use of rare earths in wind turbines", *Resources Policy*, Vol. 52, pp. 349-357, 2017.

[33] https://en.institut-seltene-erden.de/aktuelle-preise-von-seltenen-erden/ (last viewed: 15/12/2020).

[34] T. Graf, S. S. P. Parkin and C. Felser, "Heusler Compounds—A Material Class With Exceptional Properties", *IEEE Trans. Mag.*, Vol. 47(2), pp. 367-373, 2011.

[35] M. Gueltig, H. Ossmer, M. Ohtsuka, H. Miki, K. Tsuchiya, T. Takagi et al., " High Frequency Thermal Energy Harvesting Using Magnetic Shape Memory Films", *Adv. Energy Mater.*, Vol. 4, #1400751, 2014.

[36] Y. Q. Ma, C. B. Jiang, G. Feng and H. B. Xu, "Thermal stability of the $Ni_{54}Mn_{25}Ga_{21}$ Heusler alloy with high temperature transformation", *Scripta Materialia*, vol. 48, pp. 365–369, 2003.

[37] E. T. Dilmieva, Y. S. Koshkid'ko, V. V. Koledov, V. V. Khovaylo, J. Cwik, V. G. Shavrov et al., "Role of magnetic and temperature cycling on martensite formation in $Ni_{2.19}Mn_{0.81}Ga$ single crystals of a Heusler alloy", *J. Appl. Phys.*, vol. 127, 175103, 2020.

[38] X. Liang, F. Xiao, X. Jin, T. Fukuda and T. Kakeshita, "Suppression of Martensitic Transformation in $Co_2Cr(Ga,Si)$ Heusler Alloys by Thermal Cycling", *Metallurgical and Materials Transactions A*, Vol. 48A, pp. 2105-2108, 2017.

[39] D. Guyomar, G. Sebald, S. Pruvost, M. Lallart, A. Khodayari and C. Richard, "Energy Harvesting From Ambient Vibrations and Heat", *J. Intell. Mat. Syst. Struct.*, Vol. 20(5), pp. 609-624, 2009.

[40] A. Kitanovski and P. W. Egolf, "Thermodynamics of magnetic refrigeration", *Int. J. Refrigeration*, Vol. 29, pp. 3–21, 2006.

[41] DuPont™ Kapton® HN polyimide film Technical Data Sheet, https://docs.rs-online.com/c6e2/0900766b80659d8c.pdf *(last viewed: 08/05/2020)*

[42] F. Z. El Fatnani, D. Guyomar, M. Mazroui, F. Belhora and Y. Boughaleb, "Optimization and improvement of thermal energy harvesting by using pyroelectric materials", *Optical Mater.*, Vol. 56, pp. 22–26, 2016.

[43] Kapton® HN Thermal Insulating Film, https://export.rsdelivers.com/product/dupont/kapton-film-304x200x0025mm/kapton-hn-thermal-insulating-film-304mm-x-200mm-x/5363946 *(last viewed: 08/05/2020)*

[44] https://thermtest.com/materials-database#air *(last viewed: 08/05/2020)*

[45] https://www.engineeringtoolbox.com/convective-heat-transfer-d_430.html *(last viewed: 08/05/2020)*

[46] https://thermtest.com/materials-database#nickel *(last viewed: 08/05/2020)*

[47] https://thermtest.com/materials-database#cobalt *(last viewed: 08/05/2020)*

[48] https://thermtest.com/materials-database#manganese *(last viewed: 08/05/2020)*

[49] https://thermtest.com/materials-database#indium *(last viewed: 08/05/2020)*

[50] PI Ceramics™ Material Data, https://static.piceramic.com/fileadmin/user_upload/physik_instrumente/files/datasheets/PI_Ceramic_Material_Data.pdf *(last viewed: 08/05/2020)*

[51] https://thermtest.com/materials-database#brass *(last viewed: 08/05/2020)*

[52] N. Derby and S. Olbert, "Cylindrical magnets and ideal solenoids", *Amer. J. Phys.*, Vol. 78, pp. 229-235, 2010.

[53] E. Ising, "Contribution to the Theory of Ferromagnetism", PhD thesis, *Universities of Göttingen and Hamburg*, 1924. (translation : 1925).

[54] E. Lefeuvre, A. Badel, C. Richard, L. Petit and D. Guyomar, "A comparison between several vibration-powered piezoelectric generators for standalone systems", *Sens. Act. A: Phys.*, vol. 126, pp. 405-416, 2006.

[55] D. Guyomar and M. Lallart, "Recent progresses in piezoelectric nonlinear energy harvesting and issues in small scale implementation", *Micromachines*, Vol. 2(2), pp. 274-294, 2011.

[56] E. Lefeuvre, A. Badel, C. Richard and D. Guyomar, "Piezoelectric Energy Harvesting Device Optimization by Synchronous Electric Charge Extraction", *J. Intell. Mat. Syst. Struct.*, vol. 16, pp. 865-876, 2005.

[57] https://www.enocean.com/en/products/enocean_modules/stm-330stm-331/ (last viewed: 21/12/2020).